

Physics-informed Neural Networks for the Improvement of Platform Magnetometer Measurements

Kevin Styp-Rekowski^{1,2,3}, Ingo Michaelis², Monika Korte², Claudia Stolle⁴

¹Technical University of Berlin, Berlin, Germany

²GFZ Germany Research Center for Geosciences, Potsdam, Germany

³University of Rostock, Rostock, Germany

⁴Leibniz Institute for Atmospheric Physics at the University of Rostock, Kühlungsborn, Germany

Key Points:

- A calibration procedure of platform magnetometers from non-dedicated satellite missions is presented.
- A new calibration method using physics-informed neural networks with the Biot-Savart law is introduced.
- Datasets of space-based magnetic field measurements for the GOCE and GRACE-FO satellite missions are made publicly available.

Corresponding author: Kevin Styp-Rekowski, styp@gfz-potsdam.de

Abstract

Space-based measurements of the Earth’s magnetic field with a good spatiotemporal coverage are needed to understand the complex system of our surrounding geomagnetic field. High-precision magnetic field satellite missions form the backbone for sophisticated research, but they are limited in their coverage. Many satellites carry so-called platform magnetometers that are part of their attitude and orbit control systems. These can be re-calibrated by considering different behaviors of the satellite system, hence reducing their relatively high initial noise originating from their rough calibration. These platform magnetometer data obtained from non-dedicated satellite missions complement the high-precision data by additional coverage in space, time, and magnetic local times. In this work, we present an extension to our previous Machine Learning approach for the automatic in-situ calibration of platform magnetometers. We introduce a new physics-informed layer incorporating the Biot-Savart formula for dipoles that can efficiently correct artificial disturbances due to electric current-induced magnetic fields evoked by the satellite itself. We demonstrate how magnetic dipoles can be co-estimated in a neural network for the calibration of platform magnetometers and thus enhance the Machine Learning-based approach to follow known physical principles. Here we describe the derivation and assessment of re-calibrated datasets for two satellite missions, GOCE and GRACE-FO, which are made publicly available. We achieved a mean residual of about 7 nT and 4 nT for low- and mid-latitudes, respectively.

Plain Language Summary

This study revolves around enhancing our understanding of Earth’s magnetic field by leveraging satellite data. While certain satellites provide highly detailed magnetic field information, their coverage is limited in geographical and temporal scope. Many satellites carry basic magnetic sensors as part of their control systems, but these sensors are initially rather inaccurate. We developed a sophisticated computational method that combines machine learning and physics to refine these sensor readings. Our approach specifically addresses and corrects errors stemming from the satellite’s own magnetic interference. We applied and tested this method on data from two specific satellites, namely GOCE and GRACE-FO. The improved magnetic field data resulting from our method is made publicly accessible, offering a more accurate and reliable dataset for researchers studying Earth’s magnetic field.

1 Introduction

Platform magnetometers, commonly installed on various satellites in low Earth orbit, offer a promising means to expand the spatial and temporal coverage of Earth’s magnetic field measurements from space. However, these instruments, initially not dedicated for geoscience applications, require calibration to ensure the scientific accuracy and usability of the collected data. To achieve this, gathering information about the satellite is essential to correct artificial disturbances caused by other payload systems and other influencing properties associated with the satellite.

To quantify the Earth’s magnetic field, several high-precision satellite missions have been operated. From 1999 to 2004, magnetic field data from the Ørsted mission (Neubert et al., 2001) are available. From 2000 to 2010, the CHAMP (Reigber et al., 2002) satellite mission was in orbit, followed by a gap from 2010 to 2013 where no high-precision mission measured the magnetic field. Since 2013, the Swarm constellation (Friis-Christensen et al., 2006; Olsen et al., 2013) provides again high-precision measurements. Recently, there have been ongoing efforts to complement the high-precision missions with additional data from non-high-precision or platform magnetometers with an analytical approach to the calibration. In this way, data from the GRACE, Cryosat-2, DMSP, GRACE-FO, Swarm-Echo, AMPERE, and GOCE missions have been calibrated and made pub-

65 licly available (Olsen, 2021; Olsen et al., 2020; Alken et al., 2020; Broadfoot et al., 2022;
 66 Anderson et al., 2000; Stolle, Michaelis, et al., 2021; Michaelis et al., 2022). Although
 67 having slightly higher noise these data complement dedicated magnetic field mission data
 68 well for understanding the Earth’s magnetic field variations. They enlarge the spatiotem-
 69 poral distribution, e.g., providing enhanced coverage of the altitudes or local times of mea-
 70 sured phenomena mainly of magnetospheric or ionospheric origin. Subsequent work has
 71 shown the analytical potential of these additional data (e.g., Stolle, Olsen, et al. (2021);
 72 Xiong et al. (2021); Park et al. (2020)).

73 In earlier works, we demonstrated the effectiveness of Machine Learning-based meth-
 74 ods for the calibration of platform magnetometers (Styp-Rekowski et al., 2021, 2022b;
 75 Bader et al., 2022). Leveraging Machine Learning (ML) techniques, we can adapt the
 76 magnetometer signal to compensate for artificial disturbances originating from the pay-
 77 load of the satellite. Our proposed non-linear regression approach automates the iden-
 78 tification of relevant features and their interactions, broadening the range of inputs that
 79 can be utilized. This reduces the analytical work required for the calibration of platform
 80 magnetometers, resulting in faster, more precise, and easily accessible magnetic datasets
 81 derived from non-dedicated satellite missions. These calibrated datasets are made pub-
 82 licly available, promoting broader scientific access and utilization (Styp-Rekowski et al.,
 83 2022a, 2023).

84 In this work, we propose an extension for the known approach by incorporating the
 85 physical Biot-Savart law into a neural network (NN), which results in a physics-informed
 86 neural network (PINN). This improves the modeling and correction of the impact of elec-
 87 tric current-induced artificial magnetic fields on the satellite’s magnetic measurements,
 88 as the PINN is more constrained to follow first-principle physical laws. In addition, the
 89 B-field estimates of the Average Magnetic field and Polar current System (AMPS) model
 90 (Laundal et al., 2018) are combined with the B-field estimates of the CHAOS-7 model
 91 (Finlay et al., 2020), improving the reference model of the calibration, especially for the
 92 polar regions. This extended approach is applied to the GOCE (Floberghagen et al., 2011;
 93 Drinkwater et al., 2003) and GRACE-FO (Kornfeld et al., 2019) satellite missions and
 94 their respective measurements. In the future, the proposed approach can be applied to
 95 a wider variety of satellites to improve the accuracy of their platform magnetometer mea-
 96 surements. We hope to enable other satellite operators to calibrate their magnetic in-
 97 struments, improve the quality of their data, and make additional data available to the
 98 scientific community.

99 In classic, on-ground calibration, a Helmholtz cage is used to determine the response
 100 of the magnetic field instrument to different applied magnetic fields considering differ-
 101 ent satellite states and the response of the instrument under calibration (Friis-Christensen
 102 et al., 2006). Recently, Springmann et al. (2010) described the satellite noise signals by
 103 dipoles, in terms of location, orientation, and strength, by employing multiple magne-
 104 tometers in a research facility on-ground and a least-squares minimization. In this work,
 105 we present an approach to determine a similar estimation of dipoles in-flight for single
 106 magnetometers on board a satellite through data assimilation. By having a large set of
 107 available applied strengths and measured magnetic fields, the dipoles are estimated as
 108 part of a larger optimization problem. The satellites in this study carry their magnetome-
 109 ters at the same position, which makes the localization more inaccurate. However, this
 110 configuration offers the advantage of a large amount of data, encompassing various ac-
 111 tivation strengths. Consequently, numerous data points linking electric currents with their
 112 induced magnetic fields are available for analysis.

113 Physics-informed neural networks (PINN) represent a powerful combination of tra-
 114 ditional physics-based modeling and ML-based techniques (Cuomo et al., 2022). These
 115 networks are designed to incorporate physical principles into their architecture, allow-
 116 ing them to leverage data-driven insights and fundamental laws of physics. This inno-
 117 vative method has been applied in numerous fields, from fluid dynamics and materials

118 science to geophysics and beyond, making it a promising tool for complex physical systems (Yuan et al., 2020).
119

120 We evaluate our approach on multiple levels: First, a residual analysis comparing
121 the calibration quality to our reference model is conducted, followed by a feasibility study
122 assessing the ability of the models to calibrate out-of-sample data of subsequent months.
123 This shows how the calibration could be adapted for a near real-time application. We
124 also show how disturbance sources can be extracted and analyzed utilizing the proposed
125 physics-informed approach, followed by an analysis of magnetic phenomena, namely field-
126 aligned currents (FAC) and magnetic storms, using the calibrated magnetometer data.

127 The remainder of the paper is structured as follows. Section 3 introduces the proposed
128 approach, presenting the improvements to the ML-based calibration. The results
129 of the proposed approach are described in Section 4, while section 5 summarizes our findings.
130

131 2 Data

132 The newly derived calibration method we propose is applied to two satellite mis-
133 sions, namely the GOCE mission (from 2009 to 2013) and the GRACE-FO mission (from
134 2018 and ongoing).

135 2.1 Satellite Data

136 The data collection process is very similar to previous works by Styp-Rekowski et
137 al. (2022b) for the GOCE satellite and by Styp-Rekowski et al. (2021) for the GRACE-
138 FO satellite. To summarize, all available data for the satellites are used, which means
139 any publicly available measurements taken onboard the satellites. Therefore, an inter-
140 polation onto common timestamps is needed, which was set to be the timestamps of the
141 position and attitude determination of the satellites. There has already been extensive
142 preprocessing of features in the form of One-hot encoding for textual features, removal
143 of non-informative features, addition of external features, scaling of the features to an
144 interval of $[-1, 1]$, automatic filling of missing values, removal of outliers, and magnetic
145 quiet time filtering. For more details, please refer to the previous publications. The GOCE
146 mission has been completed in 2013. Therefore, we have a completed dataset with no
147 new measurements. It sums up to about 6.4 million data points with 984 features used
148 within our calibration model. For the GRACE-FO mission, data have been collected since
149 June 2018 at a rate of 1Hz for the magnetic measurements. Together with this publi-
150 cation, the datasets until July 2023 will be published, which means about 162 million
151 data points with about 71 features.

152 The previous data collection process has been partly changed and extended. For
153 both satellite missions, the magnetic quiet time filtering based on the Kp (Matzka et al.,
154 2021) and Dst (Sugiura, 1964) indices has been replaced by a new filtering based on the
155 Hp30 (Yamazaki et al., 2022) and Dst indices. The increased granularity of a 30-minute
156 resolution, as compared to the previous 3-hour resolution, provides enhanced control over
157 the selection of filtered data points. As the Hp30 has been set up to contain the same
158 magnitudes as the Kp index, filtering for data points with $Hp30 \leq 2$ has been applied.

159 In addition, previous data have been flagged if the magnetorquer control currents
160 were applied at their maximum value, which was interpreted as the satellite being out
161 of attitude. This has been extended to mark whole batches of such occurrences in what
162 is described as a center-of-mass calibration maneuver, steering the magnetorquers with
163 the maximum and minimum control currents alternately (Cossavella et al., 2022).

164 In preparation for the PINN, it is necessary to identify the features that represent
165 electric currents onboard the satellite. For the GOCE satellite, these features have been

166 determined using a publicly available feature description list, which specifies the phys-
 167 ical units of the measurements, such as 'A' and 'mA'. In the case of the GRACE-FO satel-
 168 lite mission, features were identified based on their names, specifically by including the
 169 keyword "current" in their names. These features are subsequently standardized to a com-
 170 mon unit of Ampère and undergo no additional scaling during the feature preprocess-
 171 ing stage.

172 2.2 Reference Model

173 As a reference model for the calibration, the highly sophisticated CHAOS-7.15 model
 174 has been used, which is based on ground observatories as well as space-based measure-
 175 ments of the magnetic field, e.g., from nearly ten years worth of Swarm data (Finlay et
 176 al., 2020). The model has been evaluated at each satellite position to be calibrated and
 177 then rotated into the satellite frame. This reference model will be combined with the AMPS
 178 model by combining their respective B-field estimates into the finally used combined ref-
 179 erence model.

180 Laundal et al. (2018) introduced the AMPS model that describes the large-scale
 181 structure of the current system in the polar regions, also known as FACs. The model is
 182 based on several space weather parameters that are needed as input and can be used to
 183 calculate the present magnetic field at a certain position and time, whereby the mag-
 184 netic field is based only on these external phenomena that are not part of the CHAOS-
 185 7 model. Thus, this model is well-suited to be used in conjunction with the CHAOS-7
 186 model to enhance the quality of the used reference model. Recently, Kloss et al. (2023)
 187 have presented a similar idea to co-estimate the core field with the ionospheric field while
 188 creating models of the geomagnetic field, effectively combining the AMPS with the CHAOS-
 189 7 model during the creation of a new model. Here, we combine the AMPS and CHAOS-
 190 7 model by combining the magnetic field estimates.

191 For the introduction of the AMPS model, additional space weather properties are
 192 needed for its parametrization. Therefore, B_y , B_z of the interplanetary magnetic field
 193 (IMF), solar wind V_{sw} , the magnetic activity disturbance storm-time (Dst) index Dst ,
 194 the solar flux index $F10.7$, and the dipole tilt angle of the Earth $tilt$ have been added
 195 to the set of features that are only used for calculating the reference model values. Here,
 196 1-min data available for the space weather parameters, provided by the National Aero-
 197 nautics and Space Administration (NASA)¹, have been used where missing data are in-
 198 terpolated as the gaps are small and changes are expected continuously. As recommended
 199 by Laundal et al. (2018), the space weather parameters are smoothed with a rolling 20-
 200 minute window mean before input into the AMPS model. In addition, as the model is
 201 parameterized for the polar regions, only values polewards of 40° quasi-dipole latitude
 202 (QDLat) have been used, otherwise set to 0. Within the published datasets, the mag-
 203 netic fields of the AMPS model are provided separately from the CHAOS-7 data so the
 204 calibrated data can be investigated with either of the reference models. For the combi-
 205 nation of the CHAOS-7 and the AMPS model, the evaluated B field estimates are added
 206 and subsequently used as the reference model.

207 A larger error of the calibration results is expected at high latitudes than at mid
 208 and low latitudes due to increased ionospheric disturbances. The discrepancy can be miti-
 209 gated, however, only partly mitigated since the AMPS model contains the mean large-
 210 scale structures, whereas the satellite likewise measures large-scale and small-scale fea-
 211 tures of the FACs. Thus, the inclusion of the AMPS model improves the calibration pro-
 212 cess as the values provided by the combined model cover the mean variation at high lat-
 213 itudes.

¹ <https://omniweb.gsfc.nasa.gov/>

214 3 Physics-informed Calibration

215 Traditionally, platform magnetometer data have received a careful calibration where
 216 features were preselected and new features created based on the experience of the do-
 217 main expert (Olsen et al., 2020; Michaelis et al., 2022). These calibrations are well com-
 218 prehensible and are excellent in extrapolation or generalization tasks. Similar approaches
 219 have been applied to a variety of satellites, either calibrating the instrument directly or
 220 co-estimating the instrument calibration with a model calculation. Recently, a calibra-
 221 tion utilizing ML tools has been proposed with several advantages, like the possibility
 222 to use all available measurements on the satellite as the ML approach can select the rel-
 223 evant features for the calibration itself (Styp-Rekowski et al., 2021). In addition, non-
 224 linear interactions between measurements and the reference model are automatically found,
 225 thus yielding the possibility for an advanced calibration achieving lower remaining noise
 226 in the produced dataset.

227 3.1 Methods and Concepts

228 As presented in Styp-Rekowski et al. (2022b), there have been shortcomings in the
 229 ML approach. First, the calibration underestimates the FACs in the calibrated datasets,
 230 rendering the datasets less valuable for studying geomagnetic phenomena in high-latitude
 231 regions. Second, the previous ML model is only analyzable by techniques like SHAP (Lundberg
 232 & Lee, 2017), allowing a view into the inner workings of a black box. In addition, the
 233 generalizability of the previous models, e.g., when studying month-to-month models, could
 234 be improved. Within this work, we propose an extended approach to tackle these short-
 235 comings.

236 The modeling of FAC in high-latitude regions has been found to be associated with
 237 the distinct characteristics of the specific satellite mission’s orbit, i.e., GOCE. The com-
 238 bination of the sun-synchronous polar orbit and magnetic local times (MLT) of about
 239 6 and 18 LT for the descending and ascending orbit, respectively, the tilt angle of the
 240 Earth towards the sun, and the Earth’s rotation in combination lead to the phenomenon
 241 of the satellite flying through a larger area of shade around the south pole for the pe-
 242 riod around June solstice. The spatially limited shading of the satellite leads to a cer-
 243 tain uniqueness of the housekeeping parameters in this area. On the other hand, the FACs
 244 also appear in this area and are not part of the CHAOS-7 reference model. This fact leads
 245 to the previously purely statistically driven NN to correlate the unique property of the
 246 housekeeping data with the unique signal property of the FACs in this region, thus op-
 247 timizing for this correlation, which means that the housekeeping data are ‘misused’ to
 248 correct for the FAC signals present in the measured data.

249 Therefore, two extensive further developments of the previous approach have been
 250 developed to tackle this problem. First, as described in Section 2.2, the AMPS model
 251 by Laundal et al. (2018) is incorporated into our reference model, allowing us to include
 252 the average large-scale features of the FAC regions in our calibration for a better cali-
 253 bration result. Secondly, we will incorporate known laws from physics into the NN op-
 254 timization, ensuring that the calibration will be physically more correct instead of purely
 255 statistics-driven.

256 3.2 Physics-informed Component

257 One main contributor to the artificial disturbances relevant to the calibration of
 258 platform magnetometers is known to be electric currents flowing within the electronics
 259 system of a satellite. The disturbance mainly originates in the induced magnetic fields
 260 caused by a flowing electric current, which influences the measurements of the magne-
 261 tometers.

262 For this well-known phenomenon, the Biot-Savart Law gives a 3-dimensional rep-
 263 resentation of Ampère’s Law. As the magnetometer measurements originate from a 3d
 264 fluxgate magnetometer, the Biot-Savart law is the best fit to describe these processes in
 265 the satellite that couple the electric currents with induced disturbances in the form of
 266 magnetic fields. In a closed and compact system like a satellite, every circuit should be
 267 considered and modeled as closed. Therefore, the search focuses on approximations for
 268 dipoles of planar magnetic field-inducing coils. The Biot-Savart law for magnetic dipoles
 269 is given in its vector form in Equation (1),

$$270 \quad \vec{B}(\vec{r}, \vec{m}) = \frac{\mu_0}{4\pi} \left(\frac{3\hat{r}(\hat{r} * \vec{m}) - \vec{m}}{|\vec{r}|^3} \right) \quad (1)$$

271 with μ_0 as the permeability of free space,

$$272 \quad \mu_0 = 4\pi 10^{-7} \frac{Vs}{Am} \quad (2)$$

273 \vec{r} as the position at which the magnetic field is calculated, \hat{r} as the unit vector in the
 274 direction of \vec{r} as defined by

$$275 \quad \hat{r} = \frac{\vec{r}}{|\vec{r}|} \quad (3)$$

276 and the magnetic momentum \vec{m} , used in a similar way like by Springmann et al. (2010)
 277 and defined by Jackson (1999). The magnetic momentum \vec{m} , as defined in Equation (4),

$$278 \quad \vec{m} = IN \vec{a} \quad (4)$$

279 is the product of the electric current I , the area orthogonal vector \vec{a} which is perpen-
 280 dicular to the inner area of the coil and has the magnitude of the area itself, and the num-
 281 ber of coil windings N . When substituting Equation (3) into Equation (1) and some re-
 282 formatting, we arrive at our finally used formula in Equation (5).

$$283 \quad \vec{B}(\vec{r}, \vec{m}) = \frac{\mu_0}{4\pi} \left(\frac{3\vec{r}(\vec{m} * \vec{r})}{|\vec{r}|^5} - \frac{\vec{m}}{|\vec{r}|^3} \right) \quad (5)$$

284 With this formula, the physically exact induced magnetic field of the electric cur-
 285 rents in the satellite can be determined. There are some assumptions when using this
 286 formula to approximate the dipoles of inducing electric currents within the satellite sys-
 287 tem. For this simple form of the equation, the center of the coil is set to be at the ori-
 288 gin while the position of the induced magnetic field is calculated at the position \vec{r} , which
 289 in our case corresponds to the position of the magnetometer relative to the center of the
 290 coil. As in the calibration scenario of the satellites, the only given parameter in this equa-
 291 tion is the electric current I , which is part of the housekeeping datasets delivered together
 292 with the magnetometer data by the satellite operators, the 3-dimensional position \vec{r} and
 293 the area vector \vec{a} as well as the coil windings parameter N need to be estimated by the
 294 optimization function. We omit the winding parameter N in our estimation and set it
 295 to 1, with the goal of fewer parameters to estimate. If a coil has more than one wind-
 296 ing, the optimization would directly factor this property into the area vector since it acts
 297 as a factor for the momentum term. In addition, another assumption is to use the per-
 298 meability of free space, which is a good estimator within a satellite system.

299 For the satellite calibration within a PINN, this means that the input to the Biot-
 300 Savart layer is the electric current of a particular subsystem of the satellite, as can be
 301 seen in Figure 1 which shows the Biot-Savart layer schematically. This means that for
 302 every electric current present in the data, a separate Biot-Savart layer is instantiated with
 303 random vectors \vec{r} and \vec{a} . After calculating the result of Equation (5), which corresponds
 304 to the induced magnetic field, the field is inverted to correct for the artificial disturbance

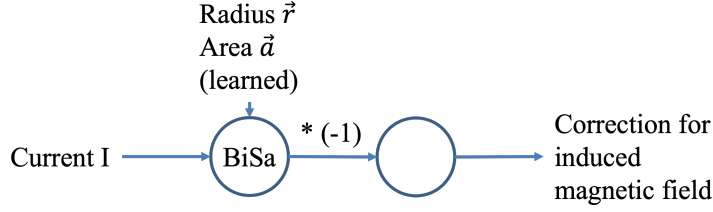


Figure 1. BiSa (Biot-Savart) layer with the electric current I as the input, learnable parameters \vec{r} and \vec{a} and the correction for the induced magnetic field.

305 introduced by the electric current being present. During the gradient-based optimization
 306 of the PINN, the learnable parameters \vec{r} and \vec{a} will be changed to match the mea-
 307 sured behavior of the satellite as a system. If an electric current present in our dataset
 308 is not relevant for the measurements of the magnetometer at hand, the \vec{a} will become
 309 very small, and the position of the coil \vec{r} will become very large relative to the mag-
 310 netometer, thus neglecting the influence of this electric current.

311 This means that the calibration becomes physically more constrained as the pro-
 312 ducing source for the induced magnetic fields is restricted to follow the Biot-Savart law.
 313 In a vanilla neural network, an arbitrary non-linear function would estimate the induced
 314 magnetic field. E.g., now a non-present electric current with a value of 0 cannot induce
 315 any magnetic field when following the equation.

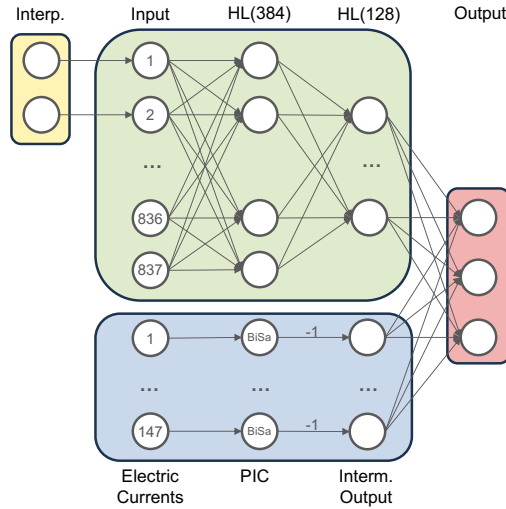


Figure 2. Architecture of the PINN calibration model for the GOCE satellite: In yellow is the time shift interpolation, in green is the FFNN, in blue is the PIC, and in red is the 3-dimensional output. The final architecture was found through a hyperparameter optimization.

316 Figure 2 shows an illustration of the architecture of the calibration model for the
 317 GOCE satellite. The architecture for the GRACE-FO is similar, with different dimen-
 318 sions for the input. The number and size of the hidden layers were determined with a
 319 hyperparameter optimization. The electric currents identified within the feature set are
 320 excluded from the feed-forward neural network (FFNN), illustrated in green, and instead

321 form the new physics-informed component (PIC), shown in blue. Within the PIC, the
 322 electric currents are translated into induced magnetic fields by the BiSa neurons and then
 323 inverted to be corrected within the last concatenation step. Finally, the 3-dimensional
 324 output layer, representing the X-, Y-, and Z-axes, illustrated in red, combines the inter-
 325 mediate outputs from the FFNN and the PIC and thus generates the final PINN cal-
 326 ibration model.

327 During the network training, the gradient of the model predictions is compared to
 328 our reference model, from which the weights and biases of the network are adjusted ac-
 329 cording to the gradient. For the PINN, this means that the location, encoded in \vec{r} , and
 330 the magnetic moment, encoded in \vec{a} , are adjusted by translating the magnetic field-related
 331 gradient into a position-related gradient, effectively adapting the relative position to fit
 332 the data. In addition, the learned parameters \vec{r} and \vec{a} are accessible in the trained model,
 333 giving the possibility for further analysis, as will be shown in Section 4.

334 With the GOCE mission providing data at 16s intervals and the GRACE-FO mis-
 335 sion providing data at 1s intervals, the model training needs to be structured. There-
 336 fore, for the GOCE mission, a global model spanning the whole mission duration (2009
 337 to 2013), and for the GRACE-FO mission, yearly models as defined by the calendar are
 338 trained. This ensures good coverage of different behaviors within the satellite as a sys-
 339 tem while, on the other hand, not exceeding computational limits in terms of memory
 340 and computation time. Afterward, the global or yearly models, respectively, are trained
 341 on a per-month basis with a much lower learning rate of $1 \cdot 10^{-5}$. Monthly data ensure
 342 enough data points for this finetuning step while enabling the models to adjust for small
 343 perturbations in the calibration over time. In addition, L1-regularization has been added
 344 with a regularization parameter of $1 \cdot 10^{-3}$ (Ng, 2004).

345 4 Evaluation

346 The proposed approach is evaluated on two satellite missions, namely the GOCE
 347 and GRACE-FO satellite missions, consisting of one and two satellites, respectively. The
 348 following subchapters show different aspects of our evaluation for either one or both mis-
 349 sions. As different housekeeping data are available, the utilized model for the two satel-
 350 lite missions looks slightly different. For the GOCE satellite, as visible in Figure 2, 837
 351 of the total 984 features are input features into the FFNN part of the PINN, while 147 fea-
 352 tures represent electric currents onboard the satellite and are fed into the PIC of the PINN.
 353 For the GRACE-FO satellite, there are nine features representing currents that are fed
 354 into the PIC of the PINN, while the other features are used in the FFNN part of the PINN.
 355 These are about 71 features, depending on the filtering applied on a yearly basis. As de-
 356 scribed in Styp-Rekowski et al. (2021) and re-evaluated in this study, the magnetome-
 357 ter readings are shifted in time by 0.67 s for the GRACE-FO1 and GRACE-FO2 satel-
 358 lites, while the magnetorquers are shifted by -0.33 s.

359 4.1 Residual Evaluation

360 In the following analysis, we restrict the data to low- and mid-latitudes and apply
 361 the filtering provided by the *BFLAG* of the dataset to restrict the evaluation to non-
 362 erroneous data as well as a $\text{Hp}30 \leq 2$ and $|Dst| \leq 30$ filtering for magnetic quiet times.

363 Looking at the residual for the GOCE mission, calculated on a per-month basis and
 364 averaged over all months, a mean absolute error (MAE) of about 6.88 nT with a stan-
 365 dard deviation (SD) of 10.41 nT was achieved, as can be seen in Table 1. For the GRACE-
 366 FO1 satellite, an MAE of about 3.62 nT with an SD of 5.22 nT, and for the GRACE-
 367 FO2, an MAE of 3.86 nT with an SD of 5.31 nT was achieved. This lies well within the
 368 margin to enable a scientific application of the proposed calibration data. In the previ-
 369 ously calibrated dataset of the GOCE satellite (Styp-Rekowski et al., 2022b), an MAE

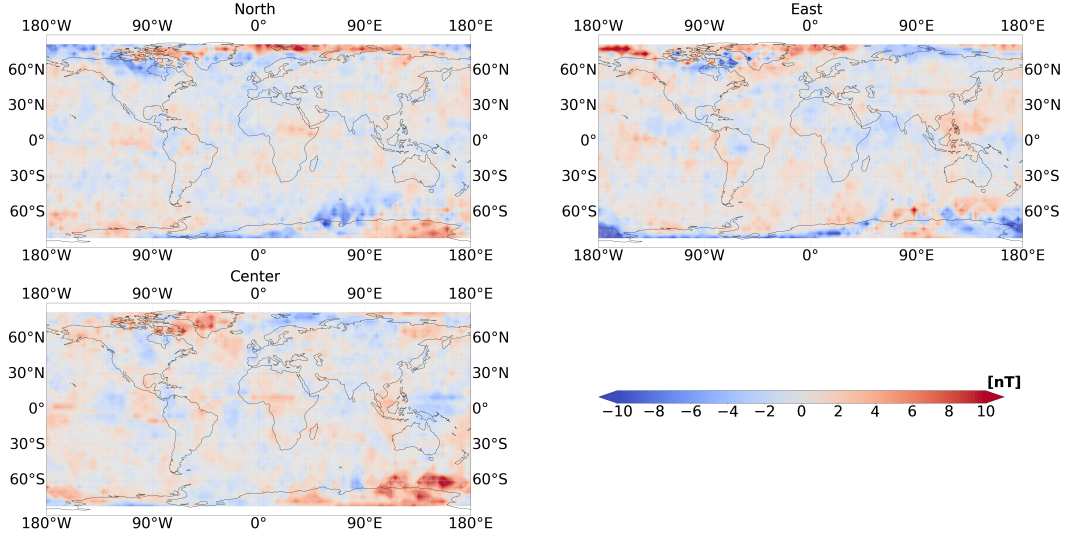


Figure 3. Residual map between the PINN calibration and the combined reference model in the NEC-frame on a scale of 10 nT with GOCE data for 2013. A grey color indicates a residual of close to 0. Note the color scale maximum and minimum values contain saturated values.

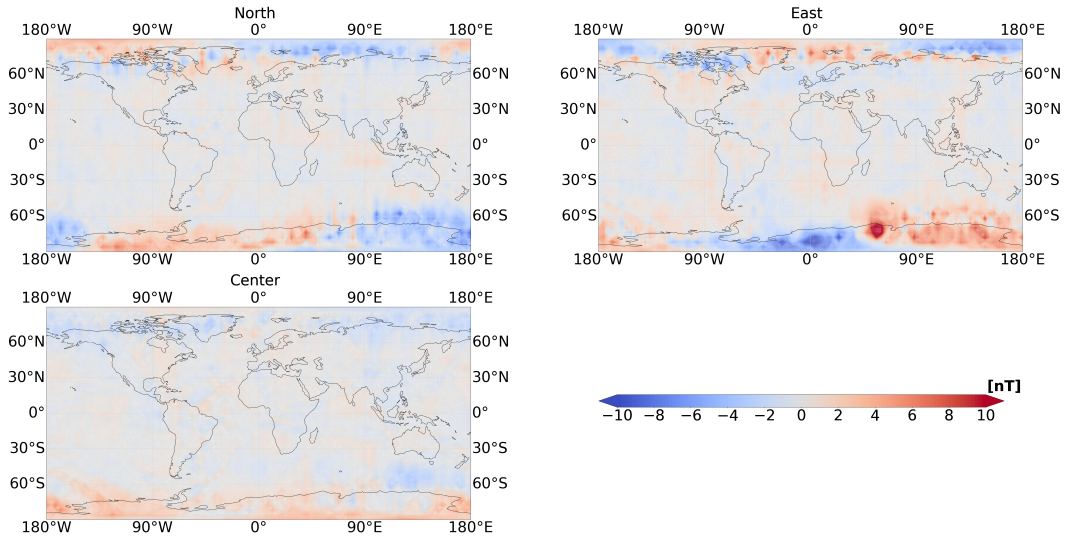


Figure 4. Residual map between the PINN calibration and the combined reference model in the NEC-frame on a scale of 10 nT with GRACE-FO1 data for 2019. A grey color indicates a residual of close to 0. Note the color scale maximum and minimum values contain saturated values.

Satellite	Mean absolute error	Standard deviation
GOCE	6.88	10.41
GRACE-FO1	3.62	5.22
GRACE-FO2	3.86	5.31

Table 1. Mean absolute error and standard deviation of the calibrated data for the different satellites, spanning the whole calibration time range.

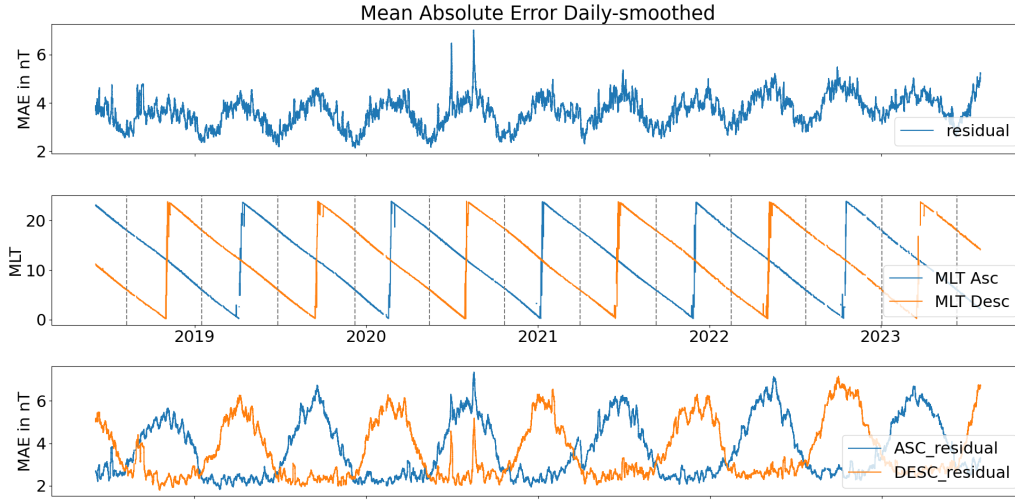


Figure 5. First row: Residual over whole calibration period for GRACE-FO1 with 86400s (daily) smoothing applied. Second row: MLT changes for the ascending and descending orbit of the mission. Dawn-dusk orbits marked with grey dotted lines for times of low residual. Third row: Same as the first row, with a separation for ascending descending orbits.

370 of 6.47 nT, of the GRACE-FO1 satellite (Styp-Rekowski et al., 2021), an MAE of about
 371 2.96 nT and of the GRACE-FO2 satellite an MAE of 3.51 nT was achieved. When compar-
 372 ing the same period as for the previous calibration of the GRACE-FO mission and
 373 GOCE mission, the new calibration has a MAE that is 0.4 nT larger than previously,
 374 which is due to the fact that the proposed calibration method is constraining the model
 375 more in the usage of the additional features. A comparison with data from the Swarm
 376 satellites is conducted in Section 4.6.

377 Exemplary, for the GOCE and GRACE-FO1 satellite, the residual data for the years
 378 2013 and 2019, respectively, have been plotted on a map of the Earth where the resid-
 379 ual has been averaged in bins of 4° latitude by 4° longitude for the contour plot in the
 380 NEC-frame. Figure 3 and Figure 4 show the result of this evaluation. With the scale given
 381 on the bottom right and the three components North, East, and Center, it can be seen
 382 that the residual has no apparent local distribution and is overall close to 0. The high-
 383 latitude areas show that the satellites measure actual data of the polar current sheets,
 384 which in average slightly differs from the given AMPS model used within the reference
 385 model.

386 By now, over five years of mission data have been acquired for the GRACE-FO satel-
 387 lite mission. This allows us to examine the behavior of the residual over a long period,
 388 spanning multiple seasons, multiple passages of the same MLTs for the satellite mission,
 389 and different levels of the solar cycle. The mean absolute residual over the whole cali-
 390 brated data of the GRACE-FO1 satellite has been plotted in Figure 5, with daily smooth-
 391 ing applied. The data have been selected for the low- and mid-latitude range with a fil-
 392 ter for the *B_FLAG* of the calibrated dataset applied and selected for magnetic quiet
 393 times using the previously defined filter. This gives an overview of how well the calibra-
 394 tion performs compared to our reference model over time. In general, there is a reap-
 395 pearing seasonality with a periodicity of about 11 months in the first panel, visible in
 396 a low residual of about 2.5 nT every 5.5 months. The second row of the plot shows how
 397 the GRACE-FO1 satellite drifts through different MLTs throughout the mission. There
 398 is a relationship between the residual and the MLT of the mission, as the satellite repeats

399 its MLT drift every 11 months, more precisely 320 days. The drops in the residual cor-
 400 relate with the dawn-dusk orbits visited by the satellite mission, where orbits with an
 401 MLT of 18 and 6 are marked with grey dotted lines.

402 Dawn, dusk and the local night time in between are the time when the least influ-
 403 ence of magnetic dayside phenomena is present. Therefore, we see the lowest residuals
 404 for dawn, dusk and night side orbits. This result is also due to the fact that the CHAOS-
 405 7 combined with AMPS reference model, does include only averaged ionospheric currents
 406 and does not capture fast, small scale variations. The third panel shows the ascending
 407 and descending residuals separately, e.g., the residual peaks are high around times when
 408 the orbit goes through a noon MLT while maintaining low residuals on the nightside.
 409 Thus, a 2-3 nT residual can be maintained if only nighttime orbits are selected. Still,
 410 daytime data should be included in our calibration and evaluation since dayside phenom-
 411 ena are of interest to the geoscientific community.

412 4.2 Predictive Calibration

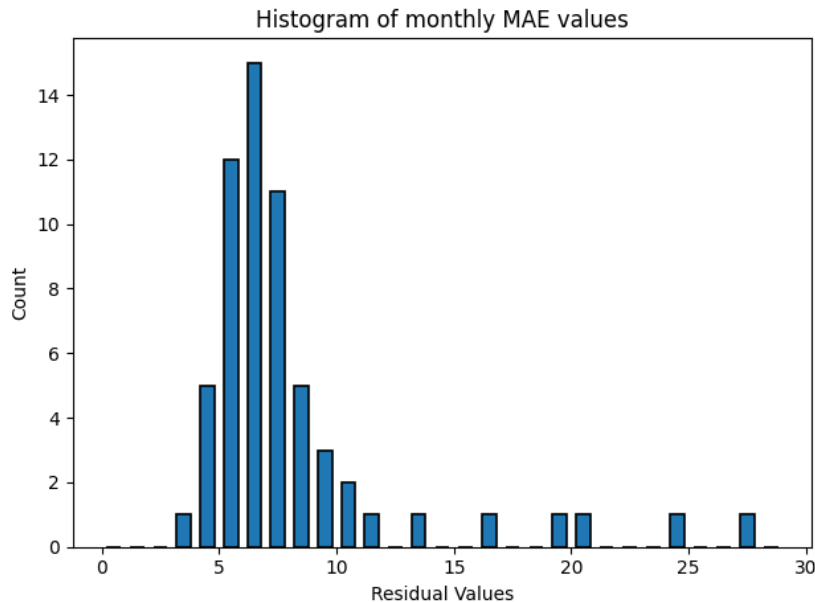


Figure 6. Histogram plot of monthly average residuals for predictive calibration models evaluated on subsequent monthly data for the whole mission data of the GRACE-FO1 satellite.

413 Additionally, a feasibility evaluation was conducted utilizing the different monthly
 414 models of the GRACE-FO1 satellite mission. For every month of the satellite mission,
 415 the calibration model that was trained on the data of the previous month has been used
 416 to calibrate the data of the current month. This is done to show how the calibrated mod-
 417 els perform on data of unseen months, which also carry a slight shift in MLT and yearly
 418 seasonality. Furthermore, this is a building block towards near real-time usage of the pro-
 419 posed calibration methods as this enables the use of precomputed models to quickly as-
 420 sess newly measured satellite data without the need for immediate training.

421 Figure 6 shows the MAE for every month calculated for low- and mid-latitudes and
 422 put into a histogram with bins of 1 nT size. Most of the residual values lie within a range
 423 of about 4 nT to 10 nT, also reflected by a median value of about 6.7 nT. There are some
 424 outliers that mainly originate from the unseen behavior of the supporting features within

425 the calibration model. Generally, the residual values are larger compared to the direct
 426 monthly calibration but remain reasonable within one order of magnitude.

427 For the potential continuous processing of GRACE-FO satellite data, two strate-
 428 gies could be deployed. A rolling yearly model could be pre-trained and applied to newly
 429 arriving monthly data, or the current yearly model could be extended by new monthly
 430 data and then fine-tuned for the latest monthly data.

431 4.3 Predicted Dipole Locations

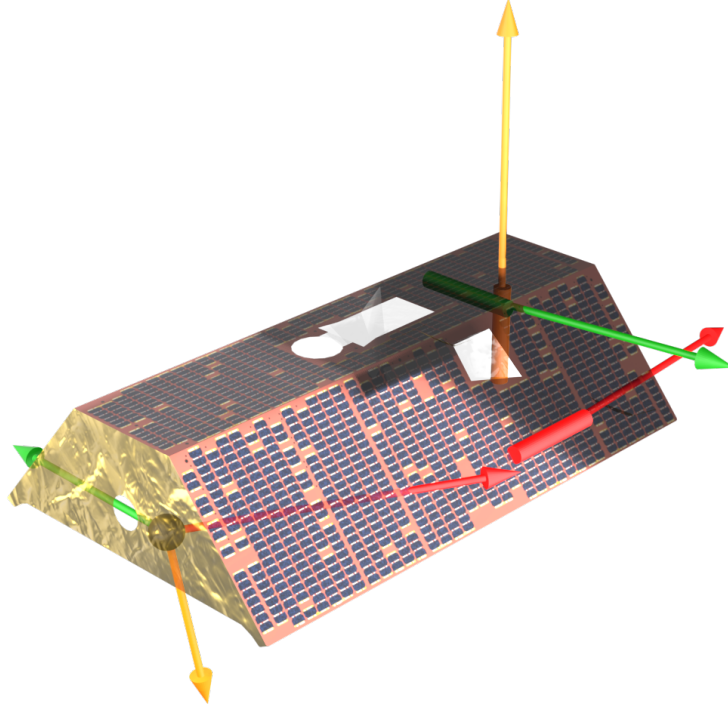


Figure 7. Model of the GRACE-FO satellite in decimeters(dm) with the magnetometer po-
 sition in front(left) of the satellite given as a black sphere. The induced magnetic field in nT
 is shown at the magnetometer position in the form of vectors. At the back of the satellite, the
 momentum at maximum control currents for the magnetorquers is given in Am^2 for the same
 magnetorquer colors, while the magnetorquers are depicted as bars with the same colors as their
 respective magnetometer axis. The momentum vectors approximately align with the X, Y, and Z
 axes of the satellite and are nearly orthogonally aligned to each other $\pm 1^\circ$.

432 As stated previously, the usage of the Biot-Savart formula within the PIC of the
 433 neural network model enables the extraction of the learned disturbance locations \vec{r}
 434 and their momentum \vec{a} if the electric current is factored in. Therefore, the maximum con-
 435 trol currents for the magnetorquers have been identified, which are about 0.109 Ampère
 436 for every magnetorquer. With these values, the induced magnetic field for the magne-
 437 tometer position can be calculated. As the Biot-Savart formula, viewed as an equations
 438 system, is underdetermined, a variety of possible \vec{r} and \vec{a} solutions are possible to achieve
 439 the same induced magnetic field at only one point within the satellite. Indeed, infinitely
 440 many solutions exist. Therefore, the induced magnetic field and the known magnetome-
 441 ter positions are taken together with the maximum current and inserted into Equation (5),
 442 and the momentum of the magnetorquers is calculated. With three given variables, the

	X	Y	Z
MTQ1	18.92	-1.67	0.29
MTQ2	1.53	15.31	0.56
MTQ3	-0.09	-0.8	18.47

Table 2. Momentum vectors for the three magnetorquers (MTQ) as derived by the learned parameters from the PINN model.

443 equation becomes a solvable linear equations system. Thus, the momentum can be ex-
444 tracted.

445 The results of this analysis can be seen in Figure 7. Here, a 3D model of the GRACE-
446 FO satellite has been rendered to visualize the results. The front of the panel, defined
447 by the direction of the laser instrument, can be seen to the left. Also, the magnetome-
448 ter is located in front of the satellite, depicted by a black sphere. The induced magnetic
449 field for the three magnetorquers is shown at the magnetometer position. Then, for the
450 approximate magnetorquer positions, as derived from construction drawings, the mag-
451 netic moment is calculated for the maximum magnetorquer control currents. These can
452 be seen in the back of the satellite. The values for the magnetorquers are also given in
453 Table 2. The table is diagonally dominated, which shows that the magnetorquer momenta
454 are mainly aligned with the X, Y, and Z-axes, while the X and Y axes show some mi-
455 nor mixing. In addition, the angles between the different momenta measure 89.3° , 90.4° ,
456 and 89.2° respectively, meaning that the momenta are approximately orthogonal.

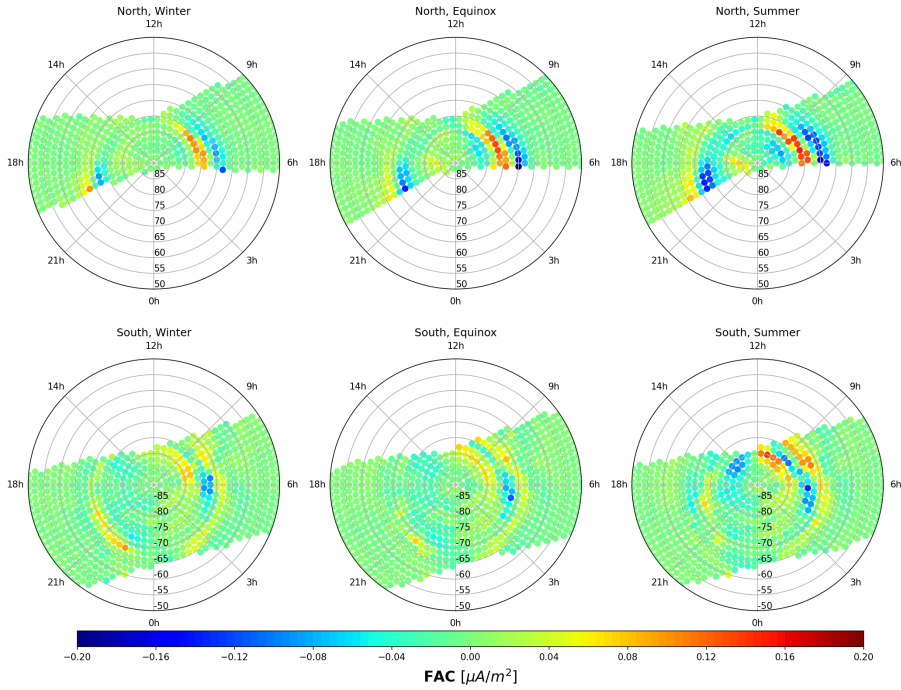
457 These results closely align with the expectations for the satellite: The three mag-
458 netorquers are built in an orthogonal fashion to enable the control of the attitude of the
459 satellite. The positions and their momenta also match with the alignment axes of the
460 built-in magnetorquer bars. This means that the PINN can reliably find and assign the
461 position and strength of the sources of artificial satellite disturbances caused by dipoles.
462 In particular, introducing PINNs can open the black box that NNs represent, allowing
463 insight into the patterns learned from the data.

464 4.4 FAC Analysis

465 To show the viability for analyzing geomagnetic phenomena, auroral FACs are in-
466 vestigated. Therefore, Figure 8 and Figure 9 show the summarized FAC in dependence
467 of the MLT and QDLat of the GOCE and GRACE-FO1 satellites, respectively. The FACs
468 have been derived from the calibrated magnetometer data and summarized by an ag-
469 gregation function into bins of 2° .

470 For the GOCE satellite, the FAC values have been aggregated by the median, while
471 for the GRACE-FO satellite, the mean could be used as it contains many more measure-
472 ments in the dataset. For both satellites, the bow-shaped Region 1 and 2 currents be-
473 come visible. This confirms that the calibration process expectedly preserves natural sig-
474 nals, and the shortcomings of the previous approach by Styp-Rekowski et al. (2022b) could
475 be overcome by introducing physical laws into the NN. Figure 8 contains a comparison
476 of the newly calibrated GOCE data with the previously published dataset. The FACs
477 in the Northern Hemisphere were less pronounced, and for the Southern Hemisphere, no
478 bow-like shapes were visible, as can be seen in the upper half of the figure. With the new
479 calibration method, this has changed drastically, and the expected shape is present in
480 the bottom half of the figure which is especially visible within the Southern Hemisphere.
481 For the GRACE-FO satellites, the result has been similar to previous studies.

GOCE FGM FAC
 2009-11-01T00:49:54.411000 - 2013-09-30T02:47:27.586000
 MLT vs QD LAT



GOCE FGM FAC
 2009-11-01T00:49 - 2013-09-30T02:47
 MLT vs QD LAT

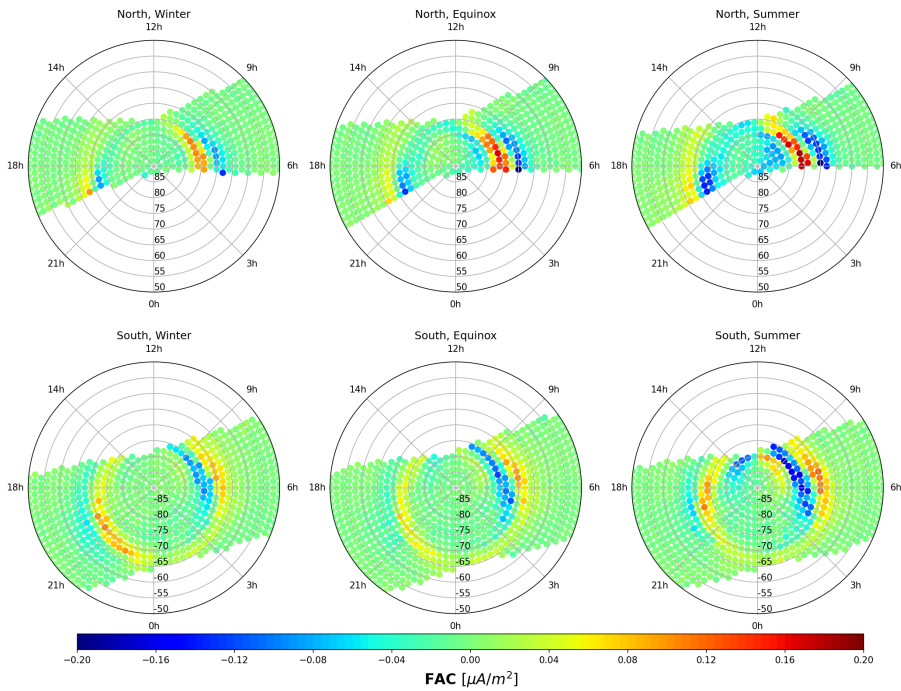


Figure 8. Field-aligned currents as derived from calibrated data of the GOCE satellite mission. Summarized median by MLT and QDLat for the Northern and Southern Hemispheres. At the top is the plot as derived from the previous approach (Styp-Rekowski et al., 2022b) and at the bottom is the newly derived plot with enhanced FACs for the Southern Hemisphere.

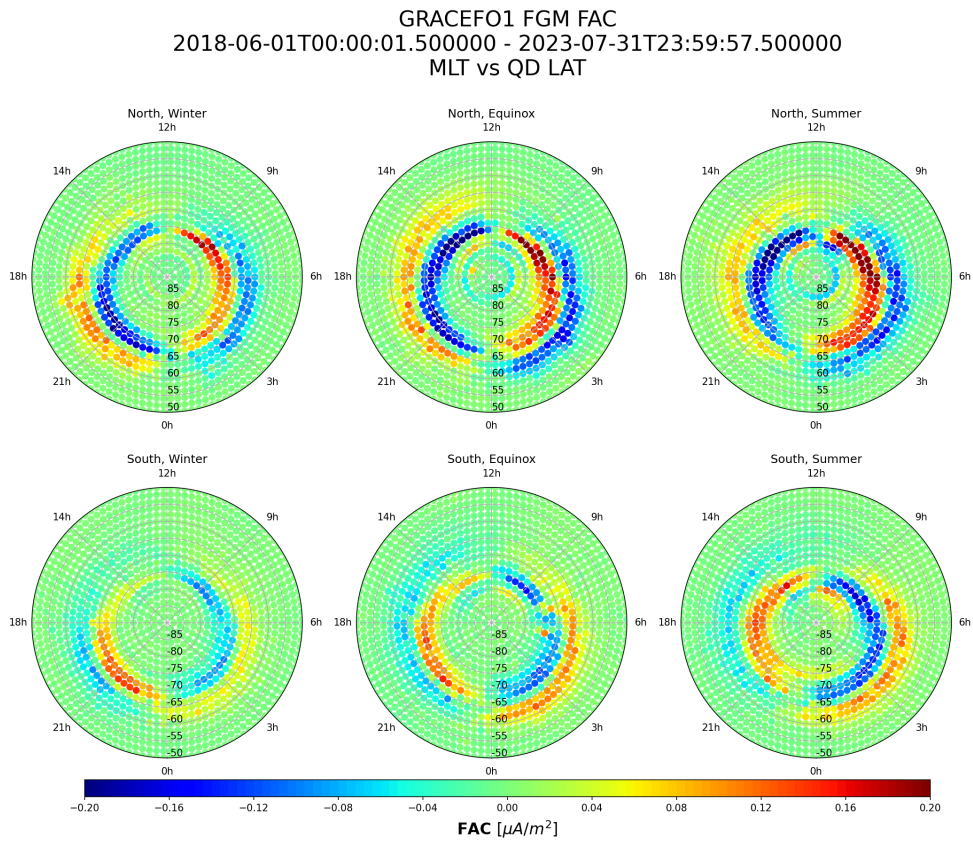


Figure 9. Field-aligned currents as derived from calibrated data of the GRACE-FO1 satellite. Summarized mean by MLT and seasons for the Northern and Southern Hemispheres.

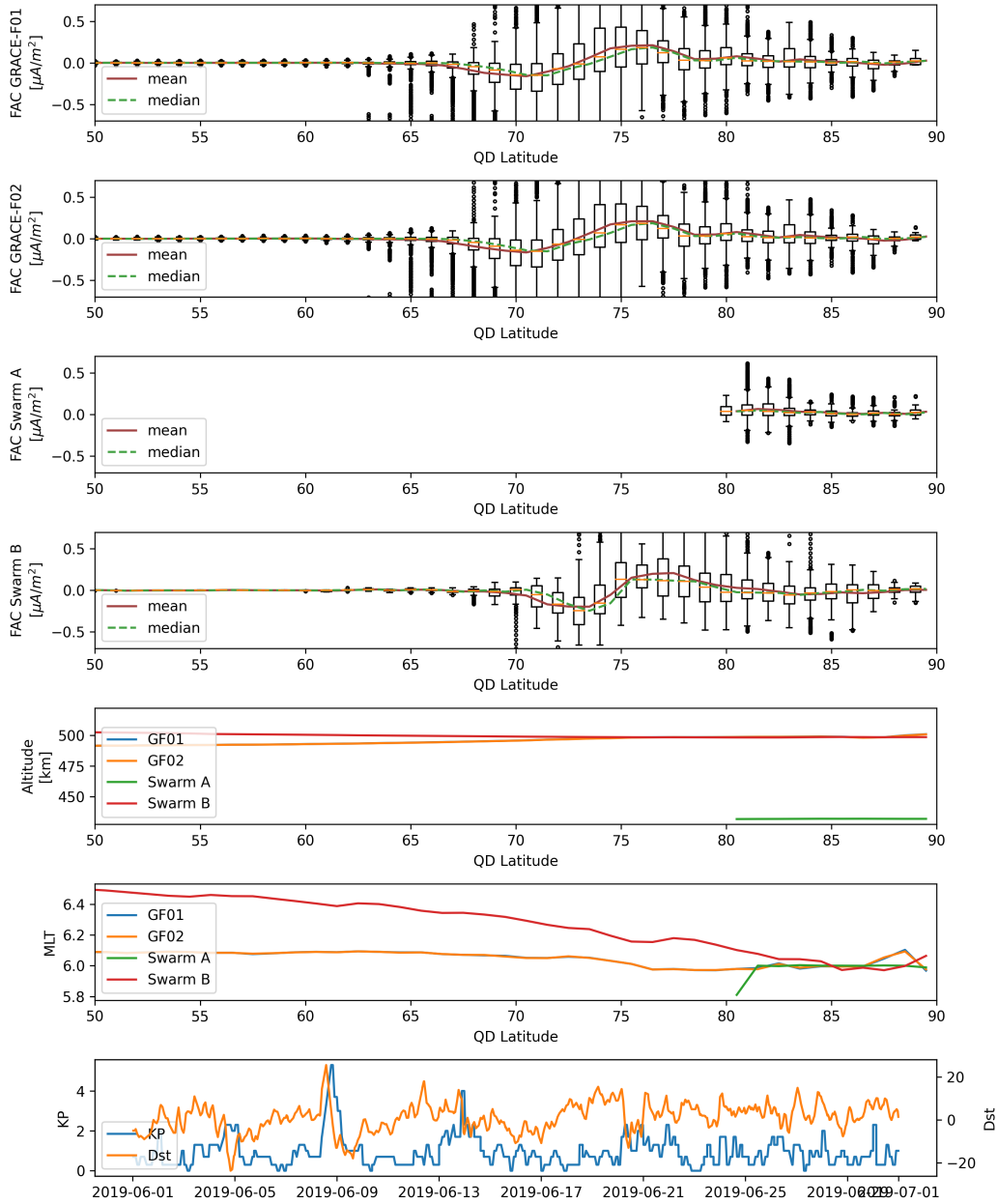


Figure 10. Boxplot summary for FAC data derived from GRACE-F01, GRACE-F02, Swarm-A, and Swarm-B missions. Data are selected from June 2019 for an MLT between 5.5 LT and 6.5 LT and quasi-dipole latitude between 50° and 90° , representing dawn. In addition, the altitude, MLT, and magnetic indices are given as mean values in dependence on quasi-dipole latitude.

482 A comparison between the GRACE-FO-derived FACs and Swarm A- and B-derived
 483 FACs has been conducted. Therefore, a slice of the MLT was taken during June 2019,
 484 ranging from MLTs of 5.5 to 6.5, representing the dawn. This choice has been made as
 485 strong currents are present during Northern Hemisphere summer for this MLT range,
 486 as seen in Figure 9.

487 The data have been low-pass filtered with a 20s cutoff similar to Xiong et al. (2021),
 488 representing large-scale FACs ($>150\text{km}$) for the GRACE-FO mission. For every degree
 489 of QDLat, the values have been summarized by a boxplot and visualized in Figure 10.
 490 In addition, the altitude, MLT, and magnetic indices are given as mean values in depen-
 491 dence on QDLat. Both GRACE-FO satellites are in good agreement with each other and
 492 capture similar structures as the Swarm satellites. Remaining differences can be attributed
 493 to the MLT of the satellites and the noise level of the calibrated GRACE-FO platform
 494 magnetometer data. Thus, the usage of calibrated GRACE-FO magnetic data to sup-
 495 port measurements by the Swarm satellite is encouraged for investigations of magnetic
 496 phenomena on a global scale.

497 4.5 Multi-mission orbit constellations

498 As an example of the application of calibrated GRACE-FO data, a recent geomag-
 499 netic storms has been investigated. The analyzed storm occurred on the 4th of Novem-
 500 ber 2021, shown in Figure 11 for four days around the high geomagnetic activity. The
 501 distribution of FAC values in dependence of QDLat and MLT for the Northern and South-
 502 ern Hemisphere is shown. The Swarm-A and Swarm-B measurements are shown in squares,
 503 while the GRACE-FO1 measurements are given in circles. The coloring contains an al-
 504 pha value. Thus, if a circle is prominently visible on a square, the GRACE-FO measure-
 505 ments disagree with the Swarm measurements, while for an agreement, the circle visu-
 506 ally merges with the square. The figure is separated into three rows, where for every row
 507 a different H_p30 selection has been applied to visualize differences in the geomagnetic
 508 activity, ranging from low activity with $H_p30 \leq 2.0$, medium activity with $2.0 < H_p30 \leq$
 509 4.0 , to high activity with $4.0 < H_p30$.

510 The MLTs of the satellite mission strongly vary and show the strength of additional
 511 data from non-dedicated missions. The global coverage of MLTs is strongly increased
 512 by using GRACE-FO data that has nearly perpendicular MLTs as the Swarm mission
 513 for this time period. The extension of the auroral oval during storm time becomes vis-
 514 ible as the covered area within the plot is larger because of the increased spatiotemp-
 515 oral coverage, enabling a global picture during magnetic storms. The idea of improving
 516 the global coverage of geomagnetic field measurements through non-dedicated satellite
 517 missions becomes evident here.

518 4.6 Evaluation against Swarm data

519 As the GRACE-FO mission has been operating since 2018 and the Swarm mission
 520 has been in orbit since 2013. Thus, the comparison between the calibrated GRACE-FO
 521 data and the data provided by the Swarm mission is possible, which is not the case for
 522 GOCE, since GOCE did not operate simultaneously with Swarm.

523 Therefore, the residuals between the Swarm and GRACE-FO1 data against their
 524 respective CHAOS-7 model prediction for low- and mid-latitudes during geomagnetic quiet
 525 times have been compared. Figure 12 shows a histogram of the North, East, and Cen-
 526 ter components of the vector magnetic field measurements for both missions. The data
 527 have been filtered with their respective flags and adjusted for the same amount of data
 528 points. The Swarm data used in this study were downloaded in October 2023 from the
 529 VirES platform (Smith et al., 2023).

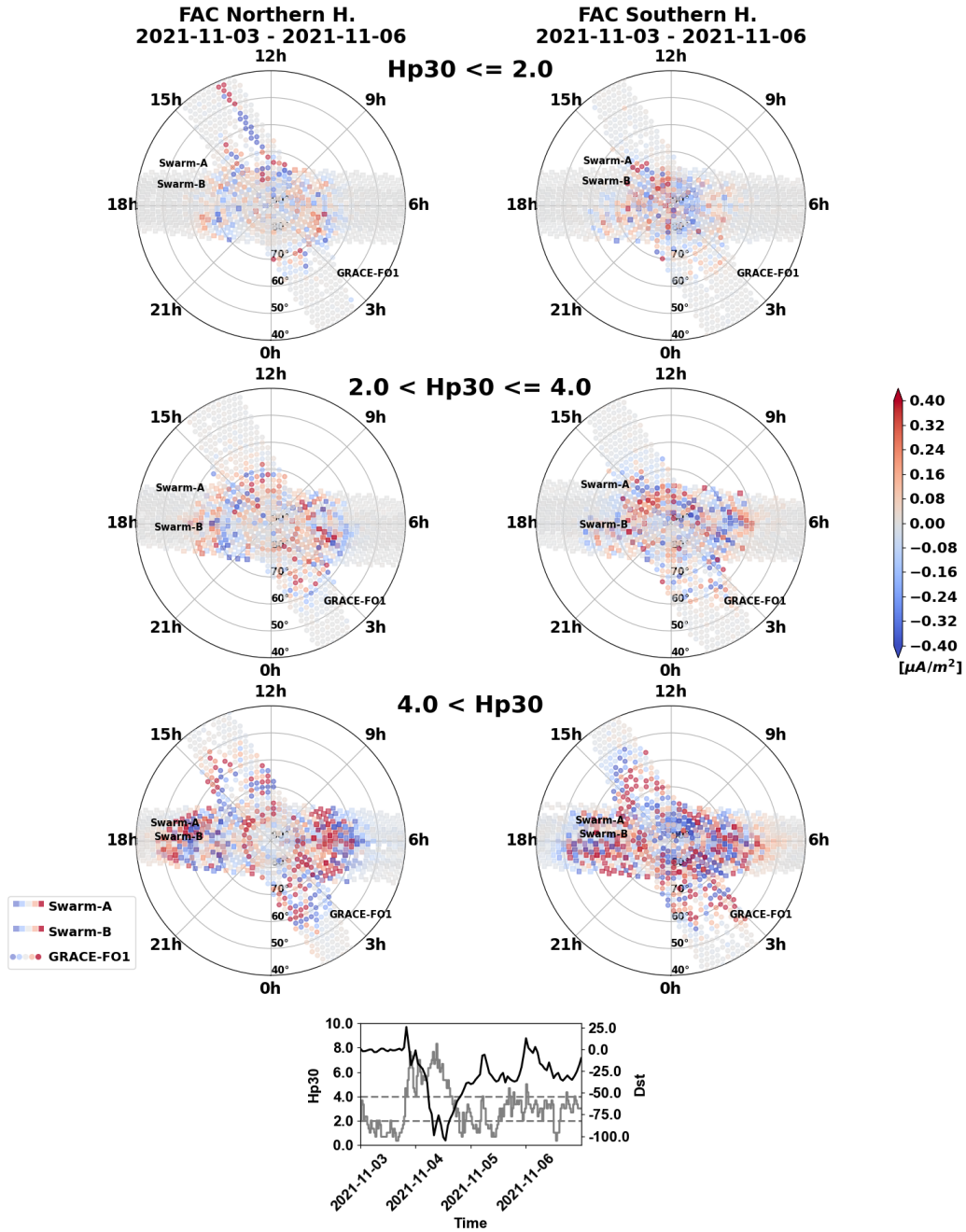


Figure 11. The mean FAC values for the Swarm-A, Swarm-B, and GRACE-FO satellite missions around the magnetic storm of the 4th of November, 2021, shown for four days, in dependence of magnetic local time and quasi-dipole latitude. The plot is divided into three rows, depending on the Hp30 index. Additionally, the Hp30 and *Dst* indices for this time frame are given.

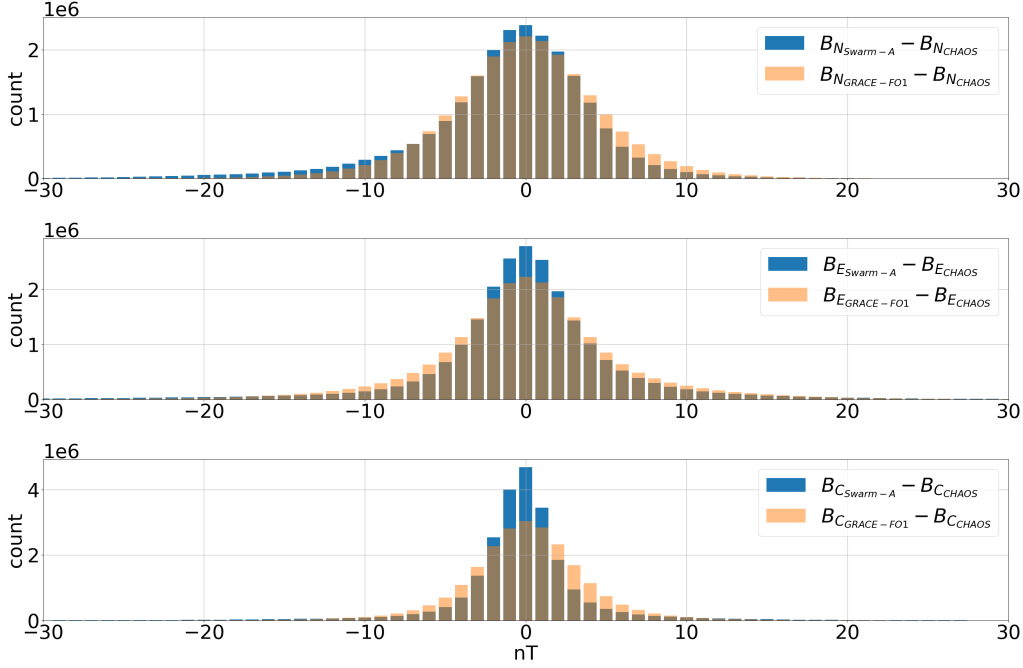


Figure 12. Residual distribution comparison of the Swarm (blue) and GRACE-FO1 (orange) calibrated data compared to the CHAOS7 reference model for the whole period from June 2018 to July 2023 within a histogram plot with bin sizes of 1 nT for the magnetic North (top), East (middle) and Center (bottom) component. Note the different vertical scales.

530 With Swarm as the high-precision mission achieving a steeper Gaussian distribu-
 531 tion, it can be seen how a significant intersection of calibrated platform magnetometer
 532 data achieves similarly low residuals. The best result was achieved for the North
 533 component. This highlights the potential of platform magnetometer data to accompany high-
 534 precision missions with additional data of only modestly higher noise. Still, it needs to
 535 be emphasized that the calibration of platform magnetometer data would not be possi-
 536 ble without a high-precision mission in space to act as a reference point because non-
 537 dedicated satellites mostly do not carry absolute magnetometers.

538 In addition, all conjunctions between the GRACE-FO1 satellite and the Swarm A
 539 satellite between June 2018 and July 2023 have been analyzed. Again, filtering for ge-
 540 omagnetic quiet times and flags has been applied. For both missions, their respective resid-
 541 ual with the CHAOS-7 model has been compared. The resulting conjunctions are binned
 542 by QDLat and MLT and aggregated by the mean, as shown in Figure 13. Overall, the
 543 conjunctions carry a low residual for low- and mid-latitude while having areas of larger
 544 residual around the poles. No apparent correlation is visible between QDLat or MLT for
 545 the conjunctions. Overall, this shows that the calibrated platform magnetometer data
 546 are in good agreement with the current high-precision mission in orbit.

547 5 Conclusion

548 This work introduced a major extension to the previous ML approach to calibrat-
 549 ing platform magnetometers carried by non-dedicated satellites. By introducing the phys-
 550 ical Biot-Savart law into the NN, the new PINN is able to correctly handle and identify
 551 magnetic dipoles acting within the satellite system. Additionally, the AMPS model was

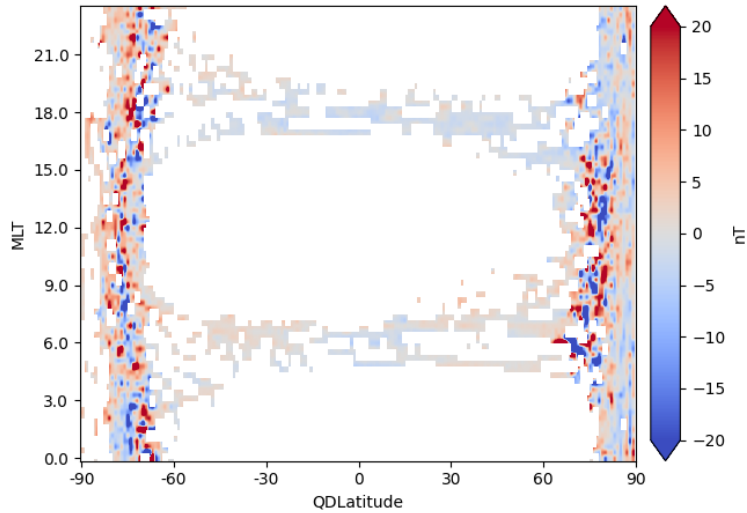


Figure 13. Conjunctions between the Swarm A and GRACE-FO1 satellites from June 2018 to July 2023. Data are selected by flags and geomagnetic quietness. The heatmap compares the residual to their respective CHAOS-7 model and shows the aggregated mean by quasi-dipole latitude and magnetic local time binning.

552 added to our reference model to anticipate large-scale auroral current system disturbance,
 553 increasing the calibration quality, particularly in the polar regions. When applied to the
 554 two satellite missions, GOCE and GRACE-FO1 together with GRACE-FO2, mean absolute
 555 residual values of 6.88 nT, 3.63 nT, and 3.86 nT could be obtained, respectively.
 556 These results enable the application of the calibrated data to analyze geomagnetic phe-
 557 nomena, as was shown exemplarily for FACs and geomagnetic storms. By its nature, this
 558 approach is mostly automated, so that it is straightforward to apply it to the calibra-
 559 tion of magnetometer data from other non-dedicated satellites in the future. The dataset
 560 of the two missions calibrated alongside this work is available (Styp-Rekowski et al., 2022a,
 561 2023).

562 Acronyms

563 **AMPS** Average Magnetic field and Polar current System
 564 **CHAMP** CHallenging Minisatellite Payload
 565 **ETL** Extract, transform, and load process
 566 **FAC** Field-aligned currents
 567 **FFNN** Feed-forward neural network
 568 **GOCE** Gravity and steady-state Ocean Circulation Explorer
 569 **GRACE** Gravity Recovery And Climate Experiment
 570 **GRACE-FO** Gravity Recovery And Climate Experiment Follow-On
 571 **IMF** Interplanetary Magnetic Field
 572 **MAE** Mean absolute error
 573 **ML** Machine Learning
 574 **MLT** Magnetic local time
 575 **MTQ** Magnetorquer
 576 **NEC** North-East-Center frame
 577 **NN** Neural network

578 **PIC** Physics-informed component
 579 **PINN** Physics-informed neural network
 580 **QDLat** Quasi-dipole latitude
 581 **SD** Standard deviation

582 Open Research Section

583 Data used in this study are publicly available from the European Space Agency (ESA)
 584 for the GOCE satellite ² and from the German Research Center for Geosciences (GFZ)
 585 for the GRACE-FO satellites (Michaelis et al., 2021). The Swarm data were accessed
 586 through the viresclient (Smith et al., 2023). The different indices and supplementary data
 587 were available from the NASA for the B_y and B_z of the IMF, the solar wind speed V_{sw} ,
 588 the Dst-index, the $F_{10.7}$ -index ³; the Hp30-index is provided by the GFZ ⁴. The refer-
 589 ence models used in this publication can be accessed through their respective publica-
 590 tions for the AMPS model (Laundal et al., 2018) and the CHAOS-7 model (Finlay et
 591 al., 2020).

592 The generated data from this publication for the calibrated geomagnetic field mea-
 593 surements, as well as their respective CHAOS-7 estimates and the derived FACs, can be
 594 found under Styp-Rekowski et al. (2022a) for the GOCE satellite and Styp-Rekowski et
 595 al. (2023) for the GRACE-FO satellites.

596 Acknowledgments

597 We thank Guram Kervalishvili, Heinz-Peter Brunke, Jan Rauberg, and Martin Rother
 598 for the vivid and fruitful discussions. This work is supported through HEIBRIDS - Helmholtz
 599 Einstein International Berlin Research School in Data Science under contract no. HIDSS-
 600 0001. This study has been partly supported by Swarm DISC activities funded by ESA
 601 under contract no. 4000109587/13/I-NB.

602 References

- 603 Alken, P., Olsen, N., & Finlay, C. C. (2020). Co-estimation of geomagnetic field
 604 and in-orbit fluxgate magnetometer calibration parameters. *Earth, Planets and*
 605 *Space*, *72*, 1–32.
- 606 Anderson, B. J., Takahashi, K., & Toth, B. A. (2000). Sensing global Birkeland
 607 currents with Iridium® engineering magnetometer data. *Geophysical Research*
 608 *Letters*, *27*(24), 4045–4048.
- 609 Bader, J., Styp-Rekowski, K., Doehler, L., Becker, S., & Kao, O. (2022). Macaw:
 610 The machine learning magnetometer calibration workflow. In *2022 IEEE inter-*
 611 *national conference on data mining workshops (icdmw)* (pp. 1095–1101).
- 612 Broadfoot, R. M., Miles, D. M., Holley, W., & Howarth, A. D. (2022). In situ cal-
 613 ibration of the Swarm-Echo magnetometers. *Geoscientific instrumentation,*
 614 *methods and data systems*, *11*(2), 323–333.
- 615 Cossavella, F., Herman, J., Hoffmann, L., Fischer, D., Save, H., Schlepp, B., & Us-
 616 beck, T. (2022). Attitude Control on GRACE Follow-On: Experiences from
 617 the First Years in Orbit. In *Space operations: Beyond boundaries to human*
 618 *endeavours* (pp. 493–517). Springer.
- 619 Cuomo, S., Di Cola, V. S., Giampaolo, F., Rozza, G., Raissi, M., & Piccialli, F.
 620 (2022). Scientific machine learning through physics-informed neural networks:

² <https://earth.esa.int/eogateway/missions/goce/data>

³ <https://omniweb.gsfc.nasa.gov/>

⁴ <https://kp.gfz-potsdam.de/hp30-hp60>

- 621 Where we are and what's next. *Journal of Scientific Computing*, 92(3), 88.
- 622 Drinkwater, M., Floberghagen, R., Haagmans, R., Muzi, D., & Popescu, A. (2003).
- 623 Vii: Closing session: Goce: Esa's first earth explorer core mission. *Space sci-*
- 624 *ence reviews*, 108(1), 419–432.
- 625 Finlay, C. C., Kloss, C., Olsen, N., Hammer, M. D., Tøffner-Clausen, L., Grayver,
- 626 A., & Kuvshinov, A. (2020). The CHAOS-7 geomagnetic field model and
- 627 observed changes in the South Atlantic Anomaly. *Earth, Planets and Space*,
- 628 72(1), 1–31.
- 629 Floberghagen, R., Fehringer, M., Lamarre, D., Muzi, D., Frommknecht, B., Steiger,
- 630 C., ... Da Costa, A. (2011). Mission design, operation and exploitation of the
- 631 gravity field and steady-state ocean circulation explorer mission. *Journal of*
- 632 *Geodesy*, 85(11), 749–758.
- 633 Friis-Christensen, E., Lühr, H., & Hulot, G. (2006, 04). Swarm: A constellation to
- 634 study the Earth's magnetic field. *Earth, planets and space*, 58, 351-358. doi:
- 635 10.1186/BF03351933
- 636 Jackson, J. D. (1999). *Classical electrodynamics* (3rd ed. ed.). New York, NY: Wiley.
- 637 Retrieved from <http://cdsweb.cern.ch/record/490457>
- 638 Kloss, C., Finlay, C. C., Laundal, K. M., & Olsen, N. (2023). Polar ionospheric
- 639 currents and high temporal resolution geomagnetic field models. *Geophysical*
- 640 *Journal International*, 235(2), 1736–1760.
- 641 Kornfeld, R. P., Arnold, B. W., Gross, M. A., Dahya, N. T., Klipstein, W. M., Gath,
- 642 P. F., & Bettadpur, S. (2019). GRACE-FO: the gravity recovery and cli-
- 643 mate experiment follow-on mission. *Journal of spacecraft and rockets*, 56(3),
- 644 931–951.
- 645 Laundal, K. M., Finlay, C. C., Olsen, N., & Reistad, J. P. (2018). Solar Wind
- 646 and Seasonal Influence on Ionospheric Currents From Swarm and CHAMP
- 647 Measurements. *Journal of Geophysical Research: Space Physics*, 123(5), 4402-
- 648 4429. Retrieved from [https://agupubs.onlinelibrary.wiley.com/doi/abs/](https://agupubs.onlinelibrary.wiley.com/doi/abs/10.1029/2018JA025387)
- 649 [10.1029/2018JA025387](https://doi.org/10.1029/2018JA025387) doi: <https://doi.org/10.1029/2018JA025387>
- 650 Lundberg, S. M., & Lee, S.-I. (2017). A unified approach to interpreting model pre-
- 651 dictions. *Advances in neural information processing systems*, 30.
- 652 Matzka, J., Stolle, C., Yamazaki, Y., Bronkalla, O., & Morschhauser, A. (2021).
- 653 The geomagnetic Kp index and derived indices of geomagnetic activity. *Space*
- 654 *weather*, 19(5), e2020SW002641.
- 655 Michaelis, I., Stolle, C., & Rother, M. (2021). *GRACE-FO calibrated and charac-*
- 656 *terized magnetometer data*. GFZ Data Services. doi: [https://doi.org/10.5880/](https://doi.org/10.5880/GFZ.2.3.2021.002)
- 657 [GFZ.2.3.2021.002](https://doi.org/10.5880/GFZ.2.3.2021.002)
- 658 Michaelis, I., Styp-Rekowski, K., Rauberg, J., Stolle, C., & Korte, M. (2022). Ge-
- 659 omagnetic data from the GOCE satellite mission. *Earth, Planets and Space*,
- 660 74(1), 1–16.
- 661 Neubert, T., Manda, M., Hulot, G., Von Frese, R., Primdahl, F., Jørgensen, J. L.,
- 662 ... Risbo, T. (2001). Ørsted satellite captures high-precision geomagnetic field
- 663 data. *Eos, Transactions American Geophysical Union*, 82(7), 81–88.
- 664 Ng, A. Y. (2004). Feature selection, l1 vs. l2 regularization, and rotational invari-
- 665 ance. In *Proceedings of the twenty-first international conference on machine*
- 666 *learning* (p. 78).
- 667 Olsen, N. (2021). Magnetometer data from the GRACE satellite duo. *Earth, Planets*
- 668 *and Space*, 73(1), 1–20.
- 669 Olsen, N., Albini, G., Bouffard, J., Parrinello, T., & Tøffner-Clausen, L. (2020).
- 670 Magnetic observations from CryoSat-2: calibration and processing of satellite
- 671 platform magnetometer data. *Earth, Planets and Space*, 72(1), 1–18.
- 672 Olsen, N., Friis-Christensen, E., Floberghagen, R., Alken, P., Beggan, C. D., Chul-
- 673 liat, A., ... others (2013). The Swarm satellite constellation application and
- 674 research facility (SCARF) and Swarm data products. *Earth, Planets and*
- 675 *Space*, 65, 1189–1200.

- 676 Park, J., Stolle, C., Yamazaki, Y., Rauberg, J., Michaelis, I., & Olsen, N. (2020). Di-
677 agnosing low-/mid-latitude ionospheric currents using platform magnetometers:
678 CryoSat-2 and GRACE-FO. *Earth, Planets and Space*, *72*, 1–18.
- 679 Reigber, C., Lühr, H., & Schwintzer, P. (2002). CHAMP mission status. *Advances in*
680 *space research*, *30*(2), 129–134.
- 681 Smith, A. R. A., Pačes, M., & Santillan, D. (2023, July). *ESA-VirES/VirES-*
682 *Python-Client*. Zenodo. Retrieved from [https://doi.org/10.5281/](https://doi.org/10.5281/zenodo.8176069)
683 [zenodo.8176069](https://doi.org/10.5281/zenodo.8176069) doi: 10.5281/zenodo.8176069
- 684 Springmann, J., Cutler, J., & Bahcivan, H. (2010). Magnetic sensor calibration and
685 residual dipole characterization for application to nanosatellites. In *Aiaa/aas*
686 *astrodynamics specialist conference* (p. 7518).
- 687 Stolle, C., Michaelis, I., Xiong, C., Rother, M., Usbeck, T., Yamazaki, Y., ... Styp-
688 Rekowski, K. (2021). Observing Earth’s magnetic environment with the
689 GRACE-FO mission. *Earth, Planets and Space*, *73*(1), 1–21.
- 690 Stolle, C., Olsen, N., Anderson, B., Doornbos, E., & Kuvshinov, A. (2021). Special
691 issue “Characterization of the geomagnetic field and its dynamic environment
692 using data from space-based magnetometers”. *Earth, Planets and Space*,
693 *73*(1), 1–4.
- 694 Styp-Rekowski, K., Michaelis, I., Korte, M., & Stolle, C. (2023). *GRACE-FO ML-*
695 *calibrated magnetic field data*. GFZ Data Services. doi: [https://doi.org/10](https://doi.org/10.5880/GFZ.2.3.2023.001)
696 [.5880/GFZ.2.3.2023.001](https://doi.org/10.5880/GFZ.2.3.2023.001)
- 697 Styp-Rekowski, K., Michaelis, I., Stolle, C., Baerenzung, J., Korte, M., & Kao, O.
698 (2022a). *GOCE ML-calibrated magnetic field data*. GFZ Data Services. doi:
699 <https://doi.org/10.5880/GFZ.2.3.2022.002>
- 700 Styp-Rekowski, K., Michaelis, I., Stolle, C., Baerenzung, J., Korte, M., & Kao, O.
701 (2022b). Machine learning-based calibration of the GOCE satellite platform
702 magnetometers. *Earth, Planets and Space*, *74*(1), 1–23.
- 703 Styp-Rekowski, K., Stolle, C., Michaelis, I., & Kao, O. (2021). Calibration of the
704 grace-fo satellite platform magnetometers and co-estimation of intrinsic time
705 shift in data. In *2021 ieee international conference on big data (big data)* (pp.
706 5283–5290).
- 707 Sugiura, M. (1964). Hourly values of equatorial Dst for the IGY. *Ann. Int. Geo-*
708 *phys.*, *35*(9).
- 709 Xiong, C., Stolle, C., Michaelis, I., Lühr, H., Zhou, Y., Wang, H., ... Rauberg, J.
710 (2021). Correlation analysis of field-aligned currents from the magnetic mea-
711 surements of GRACE follow-on mission. *Earth, Planets and Space*, *73*, 1–13.
- 712 Yamazaki, Y., Matzka, J., Stolle, C., Kervalishvili, G., Rauberg, J., Bronkalla, O.,
713 ... Jackson, D. R. (2022). Geomagnetic Activity Index Hpo. *Geophys-*
714 *ical Research Letters*, *49*(10), e2022GL098860. Retrieved from [https://](https://agupubs.onlinelibrary.wiley.com/doi/abs/10.1029/2022GL098860)
715 agupubs.onlinelibrary.wiley.com/doi/abs/10.1029/2022GL098860
716 [e2022GL098860 2022GL098860](https://doi.org/10.1029/2022GL098860) doi: <https://doi.org/10.1029/2022GL098860>
- 717 Yuan, Q., Shen, H., Li, T., Li, Z., Li, S., Jiang, Y., ... others (2020). Deep learning
718 in environmental remote sensing: Achievements and challenges. *Remote Sens-*
719 *ing of Environment*, *241*, 111716.